Effects of rarefaction in microflows between coaxial cylinders

Peyman Taheri* and Henning Struchtrup†
Department of Mechanical Engineering, University of Victoria, P.O. Box 3055, STN CSC, Victoria, British Columbia, Canada, V8W 3P6
(Received 22 May 2009; revised manuscript received 30 August 2009; published 28 December 2009)

Microscale gas flows between two rotating coaxial circular cylinders of infinite length with different temperatures are investigated. Navier-Stokes-Fourier (NSF) and regularized 13-moment (R13) equations in their linear form are used to independently analyze velocity and temperature fields in shear-driven rotary flows, i.e., cylindrical Couette flows. Knudsen boundary layers, which present non-Newtonian stress and non-Fourier heat flow, are predicted as the dominant rarefaction effects in the linear theory. We show that the R13 system yields more accurate results for this boundary value problem by predicting the Knudsen boundary layers, which are not accessible for NSF equations. Furthermore, a set of second-order boundary conditions for velocity slip and temperature jump are derived for the NSF system. It is shown that the proposed boundary conditions effectively improve the classical hydrodynamics. The accuracy of NSF and R13 equations is discussed based on their comparison with available direct simulation Monte Carlo data.

DOI: 10.1103/PhysRevE.80.066317 PACS number(s): 47.10.ab, 51.10.+y, 47.45.−n, 05.70.Ln

I. INTRODUCTION

Unlike liquid flows, a distinguishing feature of a gas flowing adjacent to a solid surface is the formation of Knudsen boundary layers [1–4]. It is well known that velocity and temperature differences between the gas and the bounding surface, and also temperature gradients along the surface can establish nonequilibrium Knudsen layers [5–8], which extend to a distance of about two mean free paths.

In gaseous flows, the degree of gas rarefaction is measured with Knudsen number Kn, the ratio of molecular mean free path to a geometric characteristic length, for example, channel width or tube radius. As the flow dimensions decrease, the Knudsen number increases and nonequilibrium effects dominate the flow, e.g., the thickness of Knudsen layer increases. As a consequence of the molecules' collisions with the boundary, the statistical molecular distribution close to the boundary deviates from the bulk distribution, where intermolecular collisions are dominant. Kinetic theory proves that this non-homogeneous statistical distribution of molecules leads to Knudsen layers [1–4], in which nonequilibrium effects such as velocity slip, temperature jump, non-Newtonian stress, and non-Fourier heat flow occur.

Circular flow between two concentric cylinders which are at different temperatures and rotate relative to each other, i.e., nonisothermal cylindrical Couette flow, is a basic problem of shear-driven flows in nonplanar coordinates. The simple configuration of cylindrical Couette flow allows to study the structure of Knudsen boundary layers over curved boundaries. Microscale cylindrical Couette flows are common in miniaturized turbomachinery designs, e.g., microturbines, where work transfer between a rotor and a fluid is desired [9]. Moreover, they have many applications in microtribology, i.e., the science of interacting surfaces in relative motion [10]. It is worth mentioning that the fast-paced growth of interest in miniaturized devices demands an accurate understanding of the underlying physical processes in microscale gaseous flows, where the rarefaction effects alter the classical flow patterns.

It is well established that nonequilibrium flows cannot properly be described by traditional hydrodynamics, namely, the Navier-Stokes-Fourier (NSF) equations [4]. Accordingly, rarefied shear-driven circular flows have been investigated experimentally [11,12] and numerically [13–23]. The numerical solutions are obtained from the Boltzmann kinetic equation using the Bhatnagar-Gross-Krook (BGK) model [24] or direct simulation Monte Carlo (DSMC) method [25]. Different aspects of these flows are studied through the kinetic approaches. These include prediction of drag coefficients on the cylinders [11,13], density minimum phenomenon [14], evaporation and condensation on the cylinders [17,20], non-Newtonian stress components [19], non-Fourier heat flow [19], flow stability [15,23], effects of boundary curvature, and the velocity inversion phenomenon [18,21,22]. The velocity inversion is a nonintuitive phenomenon which happens in cylindrical Couette flows with smooth walls. When the inner cylinder is rotating and the outer one is stationary, the velocity of the gas increases with the distance from the inner cylinder.

In Refs. [26–28] and also in the present study, it is shown that the classical NSF equations can describe some of the characteristic features of cylindrical Couette flows, e.g., velocity inversion. Moreover, they can describe the effects of velocity slip and temperature jump when higher-order boundary conditions are employed. Nevertheless, NSF equations fail to present the high-order rarefaction effects, i.e., Knudsen boundary layers.

Beside kinetic approaches, the higher-order rarefaction effects which are beyond the resolution of NSF system can be predicted by extended macroscopic transport equations [4]. Traditionally, extended macroscopic transport equations are derived from the Boltzmann kinetic equation by either the Chapman-Enskog expansion method [29] or by Grad's moment expansion [30,31]. Depending on the order of the expansions, these extended equations can be used to predict nonequilibrium effects in dilute gas flows.

*peymant@uvic.ca
†struchtr@uvic.ca

In Ref. [32], Burnett equations obtained from the Chapman-Enskog expansion method are used to examine the variations of viscosity and thermal conductivity in high-speed cylindrical Couette flows. A sever disadvantage of the Burnett-type equations is their linear instability [33,34]. Furthermore, there is no systematic approach to specify high-order derivatives of macroscopic properties on the boundary, which serve as boundary conditions for Burnett-type equations. Additionally, Khayat and Eu [35,36] adapted their Grad-type moment equations to investigate cylindrical Couette flow of Lennard-Jones fluids. However, they reduced the governing equations such that NSF boundary conditions were sufficient.

The R13 equations are a regularized version of the classical Grad's 13-moment equations [30,31]. In contrast to the Grad's system, the R13 system is able to capture the Knudsen boundary layers, which are particularly interesting in boundary-value problems of rarefied gas dynamics [37–43].

In this paper, we introduce the R13 equations and their corresponding kinetic boundary conditions as a higher-order macroscopic transport model for shear-driven rotary flows in microannuli. This model predicts a circumferential non-Fourier heat flow and non-Newtonian stress components which are pure rarefaction effects [41,42] to which little attention is given in the literature. In addition, a set of second-order boundary condition is presented, which effectively improves the NSF predictions.

We focus on radial and azimuthal momentum and heat transfer in cylindrical Couette flows, i.e., cylinders with infinite length where the effects of top and bottom surfaces are neglected. The R13 equations are applicable for flows in the transition regime where $\mathrm{Kn} \lesssim 0.5$. Both NSF and regularized 13-moment (R13) equations [4,44,45] in their linearized form are employed to solve the problem. Indeed, microflows are slow with small temperature gradients, which allow application of linear equations. The advantage of linearization is brevity of the equations, that makes the analytical solution accessible [38,41–43], on the other hand, some accuracy is lost in the linear solutions. In Sec. IV it is shown that Knudsen boundary layers which are dominant rarefaction effects in our considered problems can be estimated by the linearized R13 equations.

We conclude this introductory section by giving a short remark on stability of shear-driven rotary flows with limited axial length, also called Taylor-Couette flows. For liquids, stability of circular Couette flow with finite length is rigorously investigated by Andereck *et al.* [46]. Their experiments with water revealed that eighteen flow regimes can be distinguished in two-dimensional cylindrical Couette flows, where the effects of top and bottom ends are prominent. They showed that for fixed flow dimensions, transition between the regimes depends on the Reynolds numbers corresponding to inner and outer cylinders, and the rotation mode (counter-rotating and corotating). Experiments in [46] concern only dynamic (and not thermal) behavior of cylindrical Couette flows. To the authors' knowledge there is a lack of similar study for rarefied gas flows, owing to the difficulties of experiments with gases. However, in Refs. [15,23] DSMC simulations are reported for moderately rarefied cylindrical Couette flows without axial uniformity, where top and bottom boundaries were in effect. For a constant Knudsen number and a fixed flow geometry, they obtained three different flow regimes, which only depend on the velocity of the cylinders [23].

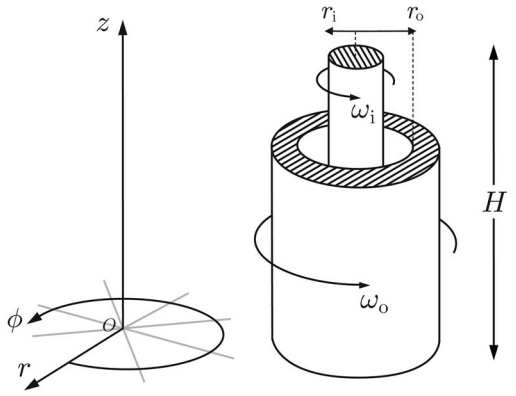

FIG. 1. Coordinates and flow setting in cylindrical Couette flow. The gas is confined in the gap between the cylinders, which have different temperatures and rotate independently.

II. PROBLEM STATEMENT

We consider a monatomic ideal-gas flow in rarefied condition that is confined in an annulus between two coaxial cylinders. The height of the cylinders H is sufficiently large such that top and bottom boundary effects can be neglected. For instance, the ratio of gap to height in the apparatus used by Alfos and Springer [11] was 0.06, where the inner and outer radii were 6.350 and 7.112 cm, respectively; the height of the cylinders was 6.350 cm, and for minimizing end effects measurements were made on the center, $H/2$.

The flow setting is depicted in Fig. 1. The temperatures of inner and outer cylinders are $T^{w,i}$ and $T^{w,o}$, respectively, where the superscript "w" refers to the properties at the cylindrical walls. The angular velocities of the cylinders are ω_i and ω_o around the z axis. We employ cylindrical coordinates $\mathbf{x}=\{r,\phi,z\}$, where r is the radial coordinate and r_i and r_o are inner and outer radii of the circular gap, respectively. The gap size is $L=r_o-r_i$. The circumferential velocities of the wall surfaces are $v_\phi^{w,i}=r_i\omega_i$, and $v_\phi^{w,o}=r_o\omega_o$. We investigate steady state behavior of the gas in the absence of body forces.

Therefore, the flows considered are defined by setting the dimensions (r_i,r_o), temperatures $(T^{w,i},T^{w,o})$, and velocities $(v_\phi^{w,o},v_\phi^{w,i})$ of the cylinders. Moreover, the gas rarefaction is controlled through the mass of the gas in the system (or the mass density at rest).

The walls are impermeable and there is no velocity in radial direction, $v_r=0$. There is no axial velocity $v_z=0$; flow is independent of axial direction $\partial/\partial z=0$, and it is uniform circumferentially, $\partial/\partial\phi=0$, i.e., axisymmetric flow. Accordingly, the velocity field reads

$$v_i=\begin{pmatrix}0\\ v_\phi(r)\\ 0\end{pmatrix}. \tag{1}$$

Since the flow is assumed to be independent of the z direction, the symmetric and trace-free stress tensor σ_{ij}, and the heat-flux vector q_i simplify to

$$\sigma_{ij}=\begin{pmatrix}\sigma_{rr}(r) & \sigma_{r\phi}(r) & 0\\ \sigma_{r\phi}(r) & \sigma_{\phi\phi}(r) & 0\\ 0 & 0 & \sigma_{zz}(r)\end{pmatrix}, \quad q_i=\begin{pmatrix}q_r(r)\\ q_\phi(r)\\ 0\end{pmatrix}, \tag{2}$$

where all components are functions of the radial coordinate r. Trace-free condition for the stress tensor gives $\sigma_{zz}(r)=-\sigma_{rr}(r)-\sigma_{\phi\phi}(r)$.

III. R13 SYSTEM FOR SHEAR-DRIVEN ROTARY FLOWS

The regularized 13-moment equations [44,45] and their corresponding boundary conditions [40] are originally presented in rectangular space (Cartesian) coordinates $\mathbf{x}=\{x,y,z\}$. It was shown that these equations can successfully describe a wealth of rarefaction effects in planar rarefied gas flows [38–43]. Particularly, formation of Knudsen boundary layers for all hydrodynamic quantities, a heat flow opposite to flow direction not driven by temperature gradient, characteristic temperature dip and Knudsen paradox in force-driven Poiseuille flow, and nonhomogeneous pressure distribution in Couette and Poiseuille flows.

In this section, we present the R13 equations in cylindrical space coordinates, where the transformed equations are simplified based on Eqs. (1) and (2). Transformation of the R13 equations from the rectangular to cylindrical coordinate follows from the standard vector and tensor analysis for general curvilinear systems [47].

A. Full R13 equations for shear-driven flows in the cylindrical coordinate

The fully nonlinear R13 equations include the main conservation laws for mass, momentum, and energy densities, which for the considered geometry read as

$$-\frac{\varrho v_\phi^2}{r}+\frac{\partial p}{\partial r}+\frac{\partial \sigma_{rr}}{\partial r}+\frac{\sigma_{rr}-\sigma_{\phi\phi}}{r}=0, \tag{3}$$

$$\frac{\partial \sigma_{r\phi}}{\partial r}+2\frac{\sigma_{r\phi}}{r}=0, \tag{4}$$

$$\frac{\partial q_r}{\partial r}+\frac{q_r}{r}=-\sigma_{r\phi}\left(\frac{\partial v_\phi}{\partial r}-\frac{v_\phi}{r}\right). \tag{5}$$

Here, ϱ is the mass density and θ is the temperature in energy units ($\theta=\mathcal{R}T$, where $\mathcal{R}$ is the gas constant and T is thermodynamic temperature). For monatomic ideal gases $p=\varrho\theta$ holds as the equation of state, where p is the pressure.

Equations (3) and (4) are the momentum balance in the radial and azimuthal directions, respectively. Equation (5) is the energy balance, where the coupling between $\sigma_{r\phi}$ and v_ϕ on the right-hand side represents the viscous heating terms. Due to the prescribed geometry, continuity and z-momentum equations turn out to be trivial.

The extended balance equations for the heat-flux components $\{q_r,q_\phi\}$ and the stress tensor components $\{\sigma_{rr},\sigma_{r\phi},\sigma_{\phi\phi}\}$ follow from their respective moment equations [4,44,45] that in cylindrical space coordinates are

$$\frac{2}{5}\left(\frac{\partial v_\phi}{\partial r}-6\frac{v_\phi}{r}\right)q_\phi-\frac{\theta\sigma_{rr}}{\varrho}\frac{\partial\varrho}{\partial r}-\frac{\sigma_{r\phi}}{\varrho}\left(\frac{\partial\sigma_{r\phi}}{\partial r}+\frac{2\sigma_{r\phi}}{r}\right)+\frac{5}{2}\sigma_{rr}\frac{\partial\theta}{\partial r}+\left(\theta-\frac{\sigma_{rr}}{\varrho}\right)\left(\frac{\partial\sigma_{rr}}{\partial r}+\frac{\sigma_{rr}-\sigma_{\phi\phi}}{r}\right)+\frac{1}{2}\left(\frac{\partial R_{rr}}{\partial r}+\frac{R_{rr}-R_{\phi\phi}}{r}\right)$$
$$+m_{rr\phi}\left(\frac{\partial v_\phi}{\partial r}-\frac{v_\phi}{r}\right)+\frac{1}{6}\frac{\partial\Delta}{\partial r}=\underline{-\frac{2}{3}\frac{p}{\mu}q_r-\frac{5}{2}p\frac{\partial\theta}{\partial r}}, \tag{6}$$

$$\frac{7}{5}\left(\frac{\partial v_\phi}{\partial r}+\frac{3}{7}\frac{v_\phi}{r}\right)q_r+\left(\theta-\frac{\sigma_{\phi\phi}}{\varrho}\right)\left(\frac{\partial\sigma_{r\phi}}{\partial r}+2\frac{\sigma_{r\phi}}{r}\right)+\sigma_{r\phi}\left(\frac{5}{2}\frac{\partial\theta}{\partial r}-\frac{\theta}{\varrho}\frac{\partial\varrho}{\partial r}\right)-\frac{\sigma_{r\phi}}{\varrho}\left(\frac{\partial\sigma_{rr}}{\partial r}+\frac{\sigma_{rr}-\sigma_{\phi\phi}}{r}\right)+\frac{1}{2}\frac{\partial R_{r\phi}}{\partial r}+\frac{R_{r\phi}}{r}$$
$$+m_{r\phi\phi}\left(\frac{\partial v_\phi}{\partial r}-\frac{v_\phi}{r}\right)=-\frac{2}{3}\frac{p}{\mu}q_\phi, \tag{7}$$

and

$$-\frac{2}{3}\left(\frac{\partial v_\phi}{\partial r}+5\frac{v_\phi}{r}\right)\sigma_{r\phi}+\frac{4}{15}\left(2\frac{\partial q_r}{\partial r}-\frac{q_r}{r}\right)+\frac{\partial m_{rrr}}{\partial r}+\frac{1}{r}m_{rrr}-\frac{2}{r}m_{r\phi\phi}=-\frac{p}{\mu}\sigma_{rr}, \tag{8}$$

$$v_\phi\left(\frac{\sigma_{rr}-2\sigma_{\phi\phi}}{r}\right)+\frac{2}{5}\left(\frac{\partial q_\phi}{\partial r}-\frac{q_\phi}{r}\right)+\sigma_{rr}\frac{\partial v_\phi}{\partial r}+\frac{\partial m_{rr\phi}}{\partial r}+\frac{2}{r}m_{rr\phi}-\frac{1}{r}m_{\phi\phi\phi}=\underline{-\frac{p}{\mu}\sigma_{r\phi}-p\left(\frac{\partial v_\phi}{\partial r}-\frac{v_\phi}{r}\right)}, \tag{9}$$

$$\frac{4}{3}\left(\frac{\partial v_\phi}{\partial r}+2\frac{v_\phi}{r}\right)\sigma_{r\phi}+\frac{4}{15}\left(2\frac{q_r}{r}-\frac{\partial q_r}{\partial r}\right)+\frac{\partial m_{r\phi\phi}}{\partial r}+\frac{3}{r}m_{r\phi\phi}=-\frac{p}{\mu}\sigma_{\phi\phi}. \tag{10}$$

The underlined terms on the right-hand side of Eqs. (6) and (9) represent Fourier and Navier-Stokes laws in classical hydrodynamics, i.e., Fourier's heat conduction and Newtonian viscous shear, where the viscosity of the gas is denoted by μ.

The extended balance Eqs. (6)–(10) can be furthermore simplified by means of the main balance laws [Eqs. (3)–(5)], but to keep generality we continue with the presented form.

The regularization procedure [4,44,45] gives the additional moments as

$$\Delta = -2\frac{\sigma_{rr}^2+\sigma_{r\phi}^2+\sigma_{\phi\phi}^2+\sigma_{rr}\sigma_{\phi\phi}}{\varrho} - 12\frac{\mu}{p}\left[\theta\left(\frac{\partial q_r}{\partial r}+\frac{q_r}{r}\right)+q_r\left(\frac{5}{2}\frac{\partial\theta}{\partial r}-\frac{\theta}{\varrho}\frac{\partial\varrho}{\partial r}\right)+\theta\sigma_{r\phi}\left(\frac{\partial v_\phi}{\partial r}-\frac{v_\phi}{r}\right)\right], \tag{11}$$

$$R_{rr} = -\frac{4}{21}\frac{\sigma_{rr}^2+\sigma_{r\phi}^2-2\sigma_{\phi\phi}^2-2\sigma_{rr}\sigma_{\phi\phi}}{\varrho} - \frac{8}{5}\frac{\mu}{p}\left[\theta\left(2\frac{\partial q_r}{\partial r}-\frac{q_r}{r}\right)+2q_r\left(\frac{\partial\theta}{\partial r}-\frac{\theta}{\varrho}\frac{\partial\varrho}{\partial r}\right)+\frac{5}{7}\theta\sigma_{r\phi}\left(\frac{\partial v_\phi}{\partial r}-\frac{v_\phi}{r}\right)\right], \tag{12}$$

$$R_{r\phi} = -\frac{4}{7}\frac{\sigma_{r\phi}\sigma_{rr}+\sigma_{r\phi}\sigma_{\phi\phi}}{\varrho} - \frac{12}{5}\frac{\mu}{p}\left[\theta\left(\frac{\partial q_\phi}{\partial r}-\frac{q_\phi}{r}\right)+q_\phi\left(\frac{\partial\theta}{\partial r}-\frac{\theta}{\varrho}\frac{\partial\varrho}{\partial r}\right)+\frac{5}{7}\theta(\sigma_{rr}+\sigma_{\phi\phi})\left(\frac{\partial v_\phi}{\partial r}-\frac{v_\phi}{r}\right)\right], \tag{13}$$

$$R_{\phi\phi} = -\frac{4}{21}\frac{\sigma_{r\phi}^2-2\sigma_{rr}^2+\sigma_{\phi\phi}^2-2\sigma_{rr}\sigma_{\phi\phi}}{\varrho} - \frac{8}{5}\frac{\mu}{p}\left[\theta\left(2\frac{q_r}{r}-\frac{\partial q_r}{\partial r}\right)-q_r\left(\frac{\partial\theta}{\partial r}-\frac{\theta}{\varrho}\frac{\partial\varrho}{\partial r}\right)+\frac{5}{7}\theta\sigma_{r\phi}\left(\frac{\partial v_\phi}{\partial r}-\frac{v_\phi}{r}\right)\right], \tag{14}$$

$$m_{rrr} = -\frac{6}{5}\frac{\mu}{p}\left[\theta\frac{\partial\sigma_{rr}}{\partial r}-\frac{2}{3}\frac{\theta}{r}(\sigma_{rr}-\sigma_{\phi\phi})-\frac{\theta\sigma_{rr}}{\varrho}\frac{\partial\varrho}{\partial r}-\frac{4}{15}q_\phi\left(\frac{\partial v_\phi}{\partial r}-\frac{v_\phi}{r}\right)\right], \tag{15}$$

$$m_{rr\phi} = -\frac{16}{15}\frac{\mu}{p}\left[\theta\left(\frac{\partial\sigma_{r\phi}}{\partial r}-\frac{7}{4}\frac{\sigma_{r\phi}}{r}\right)-\frac{\theta\sigma_{r\phi}}{\varrho}\frac{\partial\varrho}{\partial r}+\frac{2}{5}q_r\left(\frac{\partial v_\phi}{\partial r}-\frac{v_\phi}{r}\right)\right], \tag{16}$$

$$m_{r\phi\phi} = -\frac{2}{3}\frac{\mu}{p}\left[\theta\left(\frac{\partial\sigma_{\phi\phi}}{\partial r}-\frac{2}{5}\frac{\partial\sigma_{rr}}{\partial r}\right)+\frac{8}{5}\frac{\theta}{r}(\sigma_{rr}-\sigma_{\phi\phi})+\frac{\theta}{\varrho}\left(\frac{2}{5}\sigma_{rr}-\sigma_{\phi\phi}\right)\frac{\partial\varrho}{\partial r}+\frac{16}{25}q_\phi\left(\frac{\partial v_\phi}{\partial r}-\frac{v_\phi}{r}\right)\right], \tag{17}$$

$$m_{\phi\phi\phi} = -\frac{4}{5}\frac{\mu}{p}\left[\theta\left(3\frac{\sigma_{r\phi}}{r}-\frac{\partial\sigma_{r\phi}}{\partial r}\right)+\frac{\theta\sigma_{r\phi}}{\varrho}\frac{\partial\varrho}{\partial r}-\frac{2}{5}q_r\left(\frac{\partial v_\phi}{\partial r}-\frac{v_\phi}{r}\right)\right]. \tag{18}$$

In original Grad's 13-moment system the higher-order moments given in Eqs. (11)–(18) are zero. We emphasize that Eqs. (6)–(18) are derived for Maxwellian molecules [4]. The nonlinear terms with gradients result from the drift term in the Boltzmann equation, while the quadratic terms without gradients result from the bilinear collision term for Maxwell molecules [48]. In order to compare the solution of the above equations to other kinetic solutions, proper scaling needs to be applied between the underlying kinetic models. For example, comparison with the BGK model requires different factors in the above equations, see chapter 8 of the textbook [4].

It is straightforward to see that for small curvatures, i.e., when $r\to\infty$, Eqs. (3)–(18) converge to the R13 equations for Couette flow in slab geometry [42].

Classical case: in classical hydrodynamics, the balance equations for heat flux and stress [Eqs. (6)–(10)] are replaced by

$$q_r^{\mathrm{NSF}} = -\kappa\frac{\partial\theta}{\partial r}, \quad \sigma_{r\phi}^{\mathrm{NSF}} = -\mu\left(\frac{\partial v_\phi}{\partial r}-\frac{v_\phi}{r}\right),$$

$$q_\phi^{\mathrm{NSF}} = \sigma_{rr}^{\mathrm{NSF}} = \sigma_{\phi\phi}^{\mathrm{NSF}} = 0, \tag{19}$$

which are the Fourier and Navier-Stokes laws with $\kappa = 15\ \mu/4$ as the heat conductivity for ideal gases. In the limit of small Knudsen numbers Eqs. (6)–(10) reduce to Eq. (19), i.e., only the underlined terms remain. The basic conservation laws in Eqs. (3)–(5) with closure (19) construct the classical hydrodynamic system.

B. R13 boundary conditions for shear-driven flows in the cylindrical coordinate

We shall employ the kinetic boundary conditions for the R13 system [40], which were obtained based on Maxwell's boundary condition for the Boltzmann equation [49]. The boundary conditions link the moments of the gas near the wall to wall velocity v_ϕ^w and wall temperature $\theta^w = \mathcal{R}T^w$. Extensive discussions on the approach are available in the literature [30,40,49–51]. The boundary conditions for the R13 system are [40]

$$\sigma_{r\phi} = \frac{-\chi}{2-\chi}\sqrt{\frac{2}{\pi\theta}}\left[\mathcal{P}\mathcal{V}_\phi+\frac{1}{5}q_\phi+\frac{1}{2}m_{rr\phi}\right]n_r, \tag{20}$$

$$R_{r\phi} = \frac{\chi}{2-\chi}\sqrt{\frac{2}{\pi\theta}}\left[\mathcal{P}\mathcal{V}_\phi(\theta-\mathcal{V}^2+6\mathcal{T})-\frac{11}{5}\theta q_\phi-\frac{1}{2}\theta m_{rr\phi}\right]n_r, \tag{21}$$

$$q_r = \frac{-\chi}{2-\chi}\sqrt{\frac{2}{\pi\theta}}\left[2\mathcal{P}\mathcal{T} - \frac{1}{2}\mathcal{P}\mathcal{V}^2 + \frac{1}{2}\theta\sigma_{rr} + \frac{1}{15}\Delta + \frac{5}{28}R_{rr}\right]n_r, \tag{22}$$

$$m_{rrr} = \frac{\chi}{2-\chi}\sqrt{\frac{2}{\pi\theta}} \times\left[\frac{2}{5}\mathcal{P}\mathcal{T} - \frac{3}{5}\mathcal{P}\mathcal{V}^2 - \frac{7}{5}\theta\sigma_{rr} + \frac{1}{75}\Delta - \frac{1}{14}R_{rr}\right]n_r, \tag{23}$$

$$m_{r\phi\phi} = \frac{-\chi}{2-\chi}\sqrt{\frac{2}{\pi\theta}}\left[\frac{1}{5}\mathcal{P}\mathcal{T} - \frac{4}{5}\mathcal{P}\mathcal{V}^2 + \frac{1}{14}R_{\phi\phi} + \theta\left(\sigma_{\phi\phi} - \frac{1}{5}\sigma_{rr}\right) + \frac{1}{150}\Delta\right]n_r, \tag{24}$$

with

$$\mathcal{P} = p + \frac{1}{2}\sigma_{rr} - \frac{1}{120}\frac{\Delta}{\theta} - \frac{1}{28}\frac{R_{rr}}{\theta},$$

$$\mathcal{V}_\phi = v_\phi - v_\phi^w, \quad \mathcal{T} = \theta - \theta^w. \tag{25}$$

Here, velocity slip and temperature jump at the boundary are denoted by $\mathcal{V}_\phi$ and $\mathcal{T}$. The surface normal vectors on inner and outer walls are $n_r^i = +1$ and $n_r^o = -1$, respectively. The surface accommodation coefficient for macroscopic quantities is presented by χ. In theory, exact boundary conditions are available if the details of the gas-surface interaction are known. In the absence of such information, a simple argument going back to Maxwell [49] can be utilized to derive macroscopic boundary conditions for the moments. In Maxwell's diffusive-reflective boundary condition $\chi=0$ and $\chi=1$ present fully reflective (smooth) and fully diffusive (rough) surfaces, respectively. These accommodation coefficients are generally considered as surface properties and in engineering applications are very close to unity [11].

Since mass is conserved in the process, the auxiliary condition,

$$\int_{r_i}^{r_o} \varrho r\, dr = \text{const}, \tag{26}$$

can be used to find the radial density distribution.

Classical case: first- and second-order boundary conditions for velocity slip and temperature jump can be derived from the R13 boundary conditions [41]. These boundary conditions provide corrections to the zeroth-order no-slip condition, hence, their incorporation with the NSF equations allows partial compensation for the missing rarefaction effects. Based on the scaling approach in Ref. [41] these surface discontinuity conditions can be derived for cylindrical geometry as

$$\mathcal{V}_\phi^{\text{NSF}} = \underline{-\frac{2-\chi}{\chi}\sqrt{\frac{\pi\theta}{2}}\frac{\sigma_{r\phi}^{\text{NSF}}}{p}n_r} - \frac{19}{18}\frac{\sigma_{r\phi}^{\text{NSF}}q_r^{\text{NSF}}}{p^2} + \frac{1}{3}\frac{\mu\theta}{p^2}\left(\frac{5}{2}\frac{\partial\sigma_{r\phi}^{\text{NSF}}}{\partial r} - \frac{\sigma_{r\phi}^{\text{NSF}}}{r}\right) - \frac{\mu}{p^2}\left(\frac{5}{6}\sigma_{r\phi}^{\text{NSF}}v_\phi - \frac{3}{5}q_r^{\text{NSF}}\right)\frac{v_\phi}{r}, \tag{27}$$

and

$$\mathcal{T}^{\text{NSF}} = \underline{-\frac{2-\chi}{\chi}\sqrt{\frac{\pi\theta}{2}}\frac{q_r^{\text{NSF}}}{2p}n_r} - \frac{92}{175}\frac{(q_r^{\text{NSF}})^2}{p^2} + \frac{\theta(\sigma_{r\phi}^{\text{NSF}})^2}{p^2}\left[\frac{\pi}{8}\left(\frac{2-\chi}{\chi}\right)^2 - \frac{29}{245}\right] + \frac{2}{35}\frac{\mu\theta}{p^2}\left(12\frac{\partial q_r^{\text{NSF}}}{\partial r} + \frac{q_r^{\text{NSF}}}{r}\right) - \frac{\mu}{p^2}\left(\theta\sigma_{r\phi}^{\text{NSF}} + \frac{24}{35}q_r^{\text{NSF}}v_\phi\right)\frac{v_\phi}{r}, \tag{28}$$

where q_r^{NSF} and $\sigma_{r\phi}^{\text{NSF}}$ are given in Eq. (19). The underlined terms correspond to the first-order slip and jump contributions, while the others are second-order corrections. The derivation of the above boundary conditions is presented in Appendix A.

C. Dimensionless and linearized R13 equations for shear-driven flows in cylindrical coordinates

In our analysis we employ the linearized Navier-Stokes-Fourier and R13 equations in dimensionless form. Nondimensionalization and linearization are performed with respect to a reference equilibrium state, defined by $\{\varrho_0, \theta_0, v_i^0 = 0\}$. Linearized equations are applicable only for processes in vicinity of the reference equilibrium state because only linear deviations from the ground equilibrium state are included within the equations. Hence, linearized equations can be used for microflows, which in most cases are slow and are subject to small temperature gradients.

The merit of linearization is simplicity of the equations that sometimes makes the analytical solution accessible. While the rarefaction effects are known from numerical solutions of the Boltzmann equation, they appear in analytical solutions of the R13 equations. The availability of analytical solutions leads to an increased understanding of linear and nonlinear rarefaction effects. The numerical solution for the fully nonlinear system demands an appropriate numerical approach which is still in development.

The following linearized equations are presented in dimensionless form. Detailed information about dimensionless parameters is available in Appendix B. In the following dimensionless equations $\text{Kn} = \lambda_0/\ell$ is the Knudsen number at the reference state, where ℓ stands for a macroscopic reference length and $\lambda_0 = \mu_0\sqrt{\theta_0}/p_0$ is the molecular mean-free path in the reference equilibrium state. For the prescribed cylindrical geometry, the chosen reference length normally is either the radius of the inner cylinder, r_i [21], the radius of

the outer cylinder, r_o [19], or the gap width, $r_o - r_i$ [18].

Linearization leads to decoupling of velocity and temperature fields, such that Eqs. (3)–(18) and their corresponding boundary conditions (20)–(26) can be split into the following three sets:

(i) The velocity problem.

R13 case:

$$\frac{\partial \sigma_{r\phi}}{\partial r} + 2\frac{\sigma_{r\phi}}{r} = 0, \tag{29}$$

$$\frac{1}{2}\frac{\partial R_{r\phi}}{\partial r} + \frac{R_{r\phi}}{r} = -\frac{2}{3\ \mathrm{Kn}} q_\phi, \tag{30}$$

$$\frac{2}{5}\left(\frac{\partial q_\phi}{\partial r} - \frac{q_\phi}{r}\right) + \frac{\partial v_\phi}{\partial r} - \frac{v_\phi}{r} - \frac{m_{\phi\phi\phi}}{r} + \frac{\partial m_{rr\phi}}{\partial r} + 2\frac{m_{rr\phi}}{r} = -\frac{1}{\mathrm{Kn}}\sigma_{r\phi}, \tag{31}$$

with the constitutive relations

$$R_{r\phi} = -\frac{12\ \mathrm{Kn}}{5}\left(\frac{\partial q_\phi}{\partial r} - \frac{q_\phi}{r}\right),$$

$$m_{rr\phi} = -m_{\phi\phi\phi} = 4\ \mathrm{Kn}\frac{\sigma_{r\phi}}{r}, \tag{32}$$

and the linearized boundary conditions

$$\sigma_{r\phi} = -\frac{\chi}{2-\chi}\sqrt{\frac{2}{\pi}}\left(\mathcal{V}_\phi + \frac{1}{5}q_\phi + \frac{1}{2}m_{rr\phi}\right)n_r, \tag{33}$$

$$R_{r\phi} = \frac{\chi}{2-\chi}\sqrt{\frac{2}{\pi}}\left(\mathcal{V}_\phi - \frac{11}{5}q_\phi - \frac{1}{2}m_{rr\phi}\right)n_r. \tag{34}$$

While Eq. (29) is the tangential momentum balance, Eqs. (30) and (31) are linearized balance equations for tangential components of heat-flux vector [Eq. (7)] and stress tensor [Eq. (9)].

As a pure rarefaction effect, the tangential heat flow q_ϕ is not driven by a temperature gradient, which makes this problem completely independent of temperature.

Classical case: the linearized velocity problem in the Navier-Stokes-Fourier system includes the tangential momentum balance [Eq. (29)],

$$\left(\frac{\partial}{\partial r} + \frac{2}{r}\right)\left(\frac{\partial v_\phi}{\partial r} - \frac{v_\phi}{r}\right) = 0, \tag{35}$$

in which the linear Navier-Stokes law for stress was used, $\sigma_{r\phi}^{\mathrm{NSF}} = -\mathrm{Kn}(\partial_r v_\phi - v_\phi/r)$.

The linearized second-order velocity slip condition for the NSF system follows from Eq. (33), which, after substitution of Navier and Stokes law reads

$$\mathcal{V}_\phi^{\mathrm{NSF}} = \frac{2-\chi}{\chi}\sqrt{\frac{\pi}{2}}\left(\frac{\partial v_\phi}{\partial r} - \frac{v_\phi}{r}\right)\mathrm{Kn}\ n_r - \left(\frac{5}{6}\frac{\partial^2 v_\phi}{\partial r^2} - \frac{7}{6}\frac{1}{r}\frac{\partial v_\phi}{\partial r} + \frac{7}{6}\frac{v_\phi}{r^2}\right)\mathrm{Kn}^2. \tag{36}$$

(ii) The temperature problem.

R13 case:

$$\frac{\partial q_r}{\partial r} + \frac{q_r}{r} = 0, \tag{37}$$

$$\frac{4}{15}\left(2\frac{\partial q_r}{\partial r} - \frac{q_r}{r}\right) + \frac{\partial m_{rrr}}{\partial r} + \frac{m_{rrr}}{r} - 2\frac{m_{r\phi\phi}}{r} = -\frac{1}{\mathrm{Kn}}\sigma_{rr}, \tag{38}$$

$$\frac{4}{15}\left(2\frac{q_r}{r} - \frac{\partial q_r}{\partial r}\right) + \frac{\partial m_{r\phi\phi}}{\partial r} + 3\frac{m_{r\phi\phi}}{r} = -\frac{1}{\mathrm{Kn}}\sigma_{\phi\phi}, \tag{39}$$

$$\frac{5}{2}\frac{\partial \theta}{\partial r} + \frac{\partial \sigma_{rr}}{\partial r} + \frac{\sigma_{rr} - \sigma_{\phi\phi}}{r} + \frac{1}{6}\frac{\partial \Delta}{\partial r} + \frac{1}{2}\frac{\partial R_{rr}}{\partial r} + \frac{1}{2}\frac{R_{rr} - R_{\phi\phi}}{r} = -\frac{2}{3\ \mathrm{Kn}} q_r, \tag{40}$$

with the constitutive relations for its higher-order moments

$$\Delta = 0, \quad R_{rr} = -R_{\phi\phi} = \frac{24\ \mathrm{Kn}}{5}\frac{q_r}{r},$$

$$m_{rrr} = -\frac{6\ \mathrm{Kn}}{5}\left(\frac{\partial \sigma_{rr}}{\partial r} - \frac{2}{3}\frac{\sigma_{rr} - \sigma_{\phi\phi}}{r}\right),$$

$$m_{r\phi\phi} = -\frac{2\ \mathrm{Kn}}{3}\left(\frac{\partial \sigma_{\phi\phi}}{\partial r} - \frac{2}{5}\frac{\partial \sigma_{rr}}{\partial r} + \frac{8}{5}\frac{\sigma_{rr} - \sigma_{\phi\phi}}{r}\right). \tag{41}$$

The boundary conditions for the temperature problem are

$$q_r = -\frac{\chi}{2-\chi}\sqrt{\frac{2}{\pi}}\left(2\mathcal{T} + \frac{1}{2}\sigma_{rr} + \frac{1}{15}\Delta + \frac{5}{28}R_{rr}\right)n_r, \tag{42}$$

$$m_{rrr} = \frac{\chi}{2-\chi}\sqrt{\frac{2}{\pi}}\left(\frac{2}{5}\mathcal{T} - \frac{7}{5}\sigma_{rr} + \frac{1}{75}\Delta - \frac{1}{14}R_{rr}\right)n_r, \tag{43}$$

$$m_{r\phi\phi} = -\frac{\chi}{2-\chi}\sqrt{\frac{2}{\pi}}\left(\frac{1}{5}\mathcal{T} - \frac{1}{5}\sigma_{rr} + \sigma_{\phi\phi} + \frac{1}{150}\Delta + \frac{1}{14}R_{\phi\phi}\right)n_r. \tag{44}$$

Equation (37) is the linearized energy balance, where the nonlinear viscous heating terms are discarded in the linearization, compare with Eq. (5). Linearized balance equations for normal components of the stress tensor and heat-flux vector are given in Eqs. (38)–(40).

Classical case: the linearized temperature problem in the Navier-Stokes-Fourier system is the energy balance [Eq. (37)],

$$\left(\frac{\partial}{\partial r}+\frac{1}{r}\right)\frac{\partial\theta}{\partial r}=0, \tag{45}$$

in which the linear Fourier law for heat conduction was used, i.e., $q_r^{\mathrm{NSF}}=-15/4\ \mathrm{Kn}\,\partial_r\theta$.

The linearized second-order temperature jump condition for NSF system follows from Eq. (42), which after substitution of Fourier's law reads

$$T^{\mathrm{NSF}}=\frac{2-\chi}{\chi}\frac{15}{8}\sqrt{\frac{\pi}{2}}\frac{\partial\theta}{\partial r}\mathrm{Kn}\,n_r-\left(\frac{18}{7}\frac{\partial^2\theta}{\partial r^2}+\frac{3}{14}\frac{1}{r}\frac{\partial\theta}{\partial r}\right)\mathrm{Kn}^2. \tag{46}$$

(iii) The density/pressure problem.

R13 case: Equation (3) is the radial momentum balance, which governs the radial density gradient. This equation in linear form is

$$\frac{\partial\varrho}{\partial r}+\frac{\partial\theta}{\partial r}+\frac{\partial\sigma_{rr}}{\partial r}+\frac{\sigma_{rr}-\sigma_{\phi\phi}}{r}=0, \tag{47}$$

where $p=p_0(1+\varrho+\theta)$ is used as the linearized ideal-gas law, see Appendix B.

The auxiliary condition given in Eq. (26) serves to evaluate the density distribution. This condition in proper dimensionless form is

$$\int_{r_i}^{r_o}(\varrho+1)r\,dr=\mathrm{const}. \tag{48}$$

Classical case: in classical hydrodynamics where non-Newtonian stress components are zero, the density-pressure problem reduces to $\partial_r\varrho=-\partial_r\theta$.

D. Remarks on characteristic parameters

The Knudsen number $\mathrm{Kn}=\lambda_0/\ell$ in the dimensionless equations is a measure for the degree of gas rarefaction. As already mentioned, the problem allows for several choices for ℓ, namely, the gap size [18], the radius of the inner cylinder [21], or the radius of the outer cylinder [19]. Accordingly, the Knudsen number is not uniquely defined. For characterizing the degree of rarefaction one will be inclined to base the definition of Kn on the smallest of these scales, i.e., either r_i or r_o-r_i. For presenting results in dimensionless form, any choice of the reference length might be used. However, one has to be careful about the various definitions used in the literature when results of different sources are compared. When comparing to the results of other authors, we shall follow their choice of definition, otherwise we base the definition of Kn on the radius of the inner cylinder.

Apart from the Knudsen number, the processes depend on the (angular) velocities of the cylinders and their temperatures. The differences in angular velocities $(\omega_o-\omega_i)$ and in temperatures $(T^{w,o}-T^{w,i})$ are the driving forces for the processes. Dimensionless measures, e.g., the Mach number, are useful to indicate the strength of these driving forces. As explained in Appendix B, for the velocity scale we use the isothermal speed of sound, $\sqrt{\theta_0}$, which is proportional to the equilibrium speed of sound, $c=\sqrt{\gamma\theta_0}$ ($\gamma=5/3$ is the ratio of specific heats). Thus, the dimensionless velocity is related to the Mach number by $|\tilde{v}|=\mathrm{Ma}\sqrt{\gamma}$.

IV. SOLUTIONS

A. Analytical solution for the linearized velocity problem

Replacement of Eqs. (32) into Eqs. (30) and (31) leads to a compact form of the velocity problem,

$$\frac{\partial\sigma_{r\phi}}{\partial r}+2\frac{\sigma_{r\phi}}{r}=0, \tag{49}$$

$$\frac{\partial}{\partial r}\left(\frac{\partial q_\phi}{\partial r}+\frac{q_\phi}{r}\right)=\frac{5}{9\ \mathrm{Kn}^2}q_\phi, \tag{50}$$

$$\frac{\partial}{\partial r}\left(\frac{2}{5}\frac{q_\phi}{r}+\frac{v_\phi}{r}\right)=-\frac{1}{\mathrm{Kn}}\frac{\sigma_{r\phi}}{r}. \tag{51}$$

It is a straightforward task to find the general solution for Eq. (49). Equation (50) is a modified Bessel equation and its general solution consists of two linearly independent solutions, the Bessel functions $\mathcal{I}_\ell$ and $\mathcal{K}_\ell$ (with $\ell=1$ in this case). The solution for v_ϕ follows by integrating Eq. (51) and substituting the obtained solutions for $\sigma_{r\phi}$ and q_ϕ. Accordingly, the general solutions for the velocity problem are

$$\sigma_{r\phi}=\frac{\mathbf{C}_1}{r^2}, \tag{52}$$

$$q_\phi=\mathbf{C}_2\mathcal{I}_1\left(\frac{\sqrt{5}}{3\ \mathrm{Kn}}r\right)+\mathbf{C}_3\mathcal{K}_1\left(\frac{\sqrt{5}}{3\ \mathrm{Kn}}r\right), \tag{53}$$

$$v_\phi=-\frac{2}{5}q_\phi+\frac{1}{2\ \mathrm{Kn}}\sigma_{r\phi}r+\mathbf{C}_4r, \tag{54}$$

where $\mathbf{C}_1$ to $\mathbf{C}_4$ are constants that must be determined from the boundary conditions.

The underlined terms denote the linearized NSF solution, which require the boundary condition (36).

As indicated in Eq. (52), the linear solutions for the shear stress are the same for both NSF and R13 systems. The Bessel functions $\mathcal{I}_1$ and $\mathcal{K}_1$ represent the Knudsen layers which are pure rarefaction effects. The circumferential heat flow q_ϕ contributes to the velocity solution. In the linear case, the only difference between NSF and R13 arises through the Knudsen boundary layer q_ϕ, where $q_\phi^{\mathrm{NSF}}=0$. Slip velocity on the boundaries is given by the coefficient $\mathbf{C}_4$ and the Knudsen layer contribution.

B. Numerical solution for the linearized temperature problem

Due to the coupling between σ_{rr} and $\sigma_{\phi\phi}$ in Eqs. (38)–(40), an analytical solution for the temperature problem is not accessible. Thus, the linear temperature problem is solved numerically as in Ref. [40].

The linearized temperature problem given by Eqs. (37)–(40) includes four independent parameters

$\{\theta, q_r, \sigma_{rr}, \sigma_{\phi\phi}\}$ and five dependent parameters $\{\Delta, R_{rr}, R_{\phi\phi}, m_{rrr}, m_{r\phi\phi}\}$, all vary only with respect to the radial direction.

In the linear case explicit expressions are available for $\{\Delta, R_{rr}, R_{\phi\phi}\}$ [see Eq. (41)] thus, these dependent parameters can be removed from the parameters list **U** as long as they can be expressed by other dependent parameters.

After straightforward manipulations the linearized temperature problem can be written in matrix form,

$$\mathbf{I}\frac{\partial \mathbf{U}}{\partial r} = \mathbf{P}\mathbf{U}, \tag{55}$$

with the boundary conditions

$$\mathbf{U} = \mathbf{B}\mathbf{U} + \mathbf{B}_{\text{inh}}, \tag{56}$$

where **I** is the unit matrix and **U** is the parameter vector

$$\mathbf{U} = (q_r, \sigma_{\phi\phi}, m_{r\phi\phi}, m_{rrr}, \sigma_{rr}, \theta)^{\mathrm{T}}. \tag{57}$$

The vector $\mathbf{B}_{\text{inh}}$ contains the boundary properties, including the temperature and accommodation coefficients of the walls

$$\mathbf{B}_{\text{inh}} = \left(2\beta\theta^w, 0, \frac{1}{5}\beta\theta^w, -\frac{2}{5}\beta\theta^w, 0\right)^{\mathrm{T}}. \tag{58}$$

For brevity in presentation of the boundary conditions, modified accommodation factors β are introduced as

$$\beta = \frac{\chi}{2-\chi}\sqrt{\frac{2}{\pi}}. \tag{59}$$

The matrices **P** and **B** are

$$\mathbf{P} = \begin{pmatrix} -\frac{1}{r} & 0 & 0 & 0 & 0 & 0 \\ 0 & \frac{4\ \mathrm{Kn}}{3r} & -\frac{3}{2\ \mathrm{Kn}} & -\frac{1}{3\ \mathrm{Kn}} & -\frac{4\ \mathrm{Kn}}{3r} & 0 \\ -\frac{4}{5r} & -\frac{1}{\mathrm{Kn}} & -\frac{3}{r} & 0 & 0 & 0 \\ \frac{4}{5r} & 0 & \frac{2}{r} & -\frac{1}{r} & -\frac{1}{\mathrm{Kn}} & 0 \\ 0 & -\frac{2}{3r} & 0 & -\frac{5}{6\ \mathrm{Kn}} & \frac{2}{3r} & 0 \\ -\frac{4}{15\ \mathrm{Kn}} & \frac{2}{3r} & 0 & \frac{1}{3\ \mathrm{Kn}} & -\frac{2}{3r} & 0 \end{pmatrix} \tag{60}$$

and

TABLE I. Rotational modes for cylinders.

	$v_\phi^{w,i}$	$v_\phi^{w,o}$
Mode 1	0.5	0
Mode 2	0	0.5
Mode 3	0.25	0.25

$$\mathbf{B} = \begin{pmatrix} -\frac{6\ \mathrm{Kn}\ \beta}{7r} & 0 & 0 & 0 & -\frac{\beta}{2} & -2\beta \\ 0 & 1 & 0 & 0 & 0 & 0 \\ \frac{12\ \mathrm{Kn}\ \beta}{35r} & -\beta & 0 & 0 & \frac{\beta}{5} & -\frac{\beta}{5} \\ -\frac{12\ \mathrm{Kn}\ \beta}{35r} & 0 & 0 & 0 & -\frac{7\beta}{5} & \frac{2\beta}{5} \\ 0 & 0 & 0 & 0 & 1 & 0 \\ 0 & 0 & 0 & 0 & 0 & 1 \end{pmatrix}. \tag{61}$$

By using the basic central finite difference method, Eq. (55) with the boundary condition (56) is solved numerically for **U**. In the linear case, the parameters in **U** change locally, and since both **P** and **B** matrices are independent of **U**, no iteration is required in the numerical method, and the accuracy of the numerical results only depends on the grid resolution.

The general solution for Eq. (45) is

$$\theta^{\mathrm{NSF}} = \mathbf{C}_5 \ln r + \mathbf{C}_6 \tag{62}$$

that gives the radial temperature distribution for the linear NSF system. The integrating constants $\mathbf{C}_5$ and $\mathbf{C}_6$ must be determined from the boundary condition (46).

V. RESULTS AND DISCUSSION

In this section, first we present a parametric study on radial distribution of macroscopic properties in the cylindrical Couette flow of a moderately rarefied gas. Furthermore, we compare the accuracy of linear Navier-Stokes-Fourier and regularized 13-moment systems with available DSMC data in the literature.

A. Results for the velocity problem

The linear velocity problem can be characterized by Knudsen number Kn, surface accommodation factor χ, and the wall velocities v_ϕ^w or wall Mach numbers. We shall investigate the radial distributions for $\{\sigma_{r\phi}, q_\phi, v_\phi\}$ given by Eqs. (52)–(54). The radius of the inner cylinder $r_i=1$ is taken as the reference length scale, i.e., the Knudsen number is defined based on the radius of the inner cylinder, and a fixed radius ratio is considered $r_o/r_i=2$. The other parameters assume the values $\chi=\{0.02, 0.2, 0.5, 1\}$ and $\mathrm{Kn}=\{0.01, 0.05, 0.1, 0.2\}$. Rotational state of the cylinders are categorized in three modes given in Table I, such that $v_\phi^{w,i}+v_\phi^{w,o}=0.5$.

Figure 2 presents the radial distribution of shear stress, circumferential heat flux, and velocity in the annulus. The

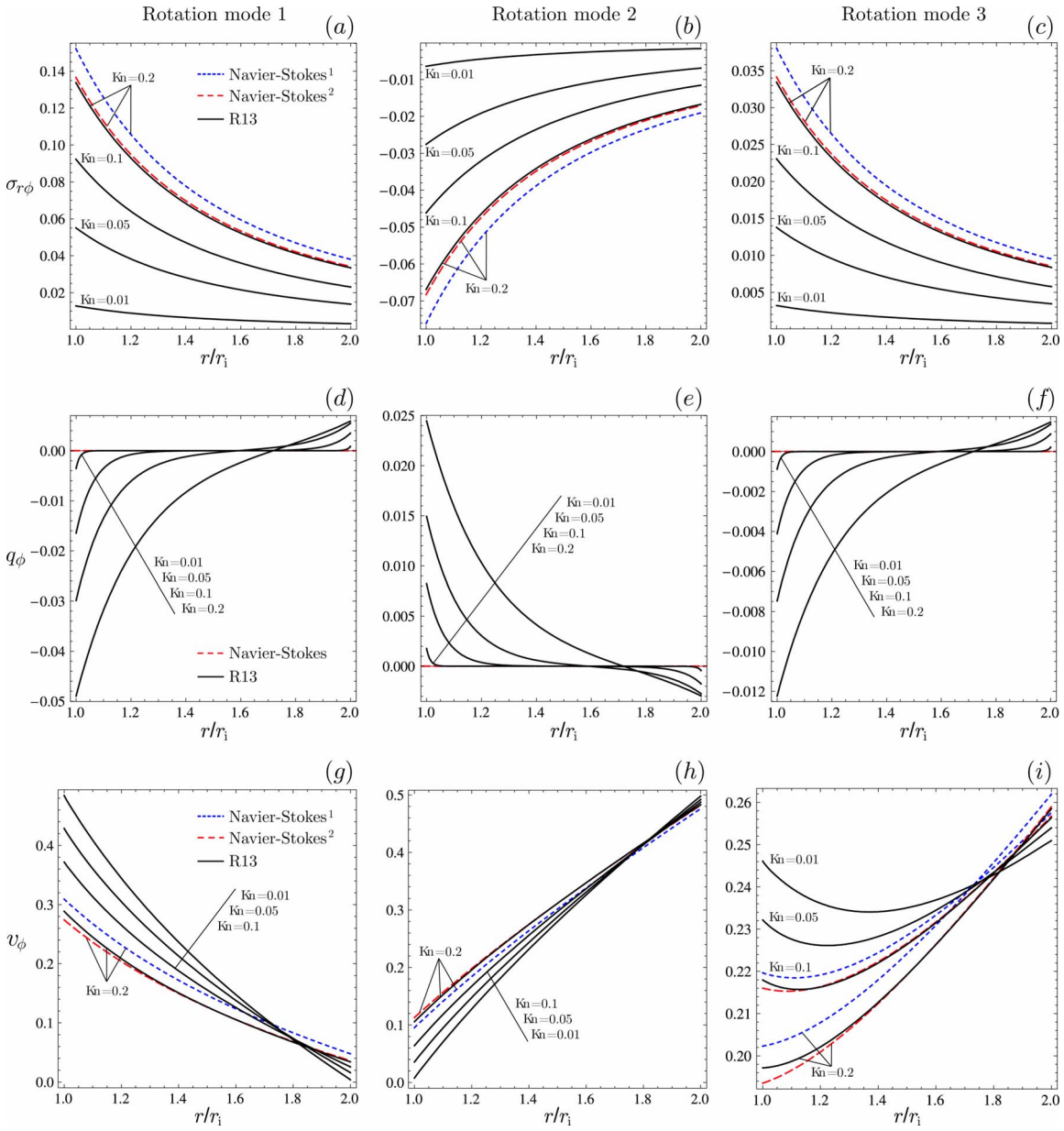

FIG. 2. (Color online) Solutions of the linear velocity problem: dashed blue line is NSF with first-order boundary condition; long-dashed red line is NSF with second-order boundary condition; continuous black line is R13 with third-order boundary conditions. Radial distribution of shear stress (top plots), circumferential heat flux (middle plots), and velocity (bottom plots) in the annulus between two fully diffusive cylinders $\chi=1$ are shown. Plots in left, middle, and right columns correspond to rotational modes 1, 2, and 3, respectively. For each rotational mode, effects of Knudsen number variation are depicted. NSF results with the proposed second-order slip condition show satisfactory agreement with the R13 predictions. For the small Knudsen numbers NSF results are not shown, since they are very close to the R13 predictions.

plots are obtained for fully diffusive walls $\chi=1$, while the effects of different Knudsen numbers and rotational modes are illustrated.

Distribution of shear stress $\sigma_{r\phi}$ for both Navier-Stokes and R13 systems is given by Eq. (52), albeit with different values for the constant $\mathbf{C}_1$, which is obtained from different boundary conditions. As shown in the top row of Fig. 2, for larger Knudsen numbers we observe larger shear stress on the walls. As expected plot (a) shows that for rotation mode 1 stress is maximum on the inner rotary cylinder and rapidly decays toward the outer stationary surface. However, this pattern is not observed for rotational mode 2 in plot (b), where the stress is minimum on the rotary outer cylinder and increases toward the inner cylinder. This occurs because of curvature effects (converging geometry), i.e., the volume of flow decreases toward the inner cylinder. Rotation of the inner cylinder in the same direction as of the outer one can change this pattern again, see plot (c).

On the middle row of Fig. 2 the circumferential heat flux given by Eq. (53) is plotted. This non-Fourier heat flow which is not driven by temperature gradient is a pure rarefaction effect and is not accessible for classical hydrodynamics,

$q_\phi^{\mathrm{NSF}}=0$. Equation (54) indicates that q_ϕ gives the Knudsen boundary layer for the velocity problem. It can be seen in Fig. 2 that the magnitude of the circumferential heat flow and thickness of the Knudsen layer increases with Kn.

As a consequence of curvature effects, for all the rotational modes the circumferential heat flow is stronger on the inner cylinder, and already for Kn=0.2 this Knudsen layer extends over the whole flow field. For rotational modes 1 and 2 the heat flow direction on the rotary wall is opposite to the wall velocity and, hence, mass flow direction. This is consistent with Couette flow simulations in planar geometry [42]. Nevertheless, in the cylindrical geometry direction of q_ϕ is inverted on the stationary walls, see plots (d) and (e) in Fig. 2.

The bottom plots in Fig. 2 are devoted to the velocity distribution. The obtained results confirm that velocity slip increases in dilute gases. Moreover, for all rotation modes, the inner cylinder has larger slip values owing to more surface curvature.

The Navier-Stokes results obtained from the first- and second-order slip conditions are shown for Kn=0.2. Indeed, the proposed higher-order boundary condition in Eq. (36) effectively shift the Navier-Stokes solutions toward the R13 prediction.

Velocity differences between R13 and NSF with second-order slip condition are more apparent near the walls. This can be explained by the explicit solution for velocity in Eq. (54) which is the superposition of Knudsen layer (q_ϕ), bulk velocity, and slip. The R13 equations benefit the Knudsen layer to provide more curvature near the walls, see plots (g) and (i) in Fig. 2.

The effects of different accommodation factors and rotational modes for Kn=0.1 are investigated in Fig. 3, where radial distribution for shear stress, circumferential heat flux, and velocity are given. Comparison between Figs. 2 and 3 shows that for the same rotational mode, variations in χ and Kn have similar effects on $\sigma_{r\phi}$ and q_ϕ distribution. Smooth walls with small χ values impose less stress and weak Knudsen layers.

In plot (g) velocity inversion is observed, i.e., flow velocity increases close to the stationary wall [18,21,26,27]. The velocity inversion takes place only for rotational mode 1 and for small accommodation coefficients. It is not a rarefaction effect as it can be predicted by NSF system. This phenomenon is the effect of curvature on the slip length, hence it cannot be observed in the planar Couette flows. In other words, cooperation between the wall curvature and wall smoothness on the inner cylinder extensively increases the slip such that velocity inversion occurs.

In Figs. 4 and 5 we have compared our velocity results with DSMC data from Refs. [18,21]. The DSMC method [25] is known as the most successful method for the solution of the Boltzmann equation. In the considered DSMC simulations, molecules are treated as hard-sphere molecules, which is consistent with the underlying kinetic of the presented R13 equations [Eq. (3)–(18)]. It is important to emphasize that in Refs. [18,21] the Knudsen number is defined based on the gap size L and inner radius r_i, respectively. Consequently, our solutions are characterized by two different Knudsen numbers.

The DSMC data in Ref. [18] are for argon at $p=101\ 325$ Pa, confined between two isothermal walls at $T=298.15$ K, where the mean-free path for hard-sphere molecules is $\lambda^{\mathrm{HS}}=6.25\times10^{-8}$ m and speed of sound is 321.626 m/s. The outer cylinder is stationary while the inner one rotates at $\omega_i=5.17\times10^8$ rad/s. The gap size is $L=r_o-r_i$ with $r_i=3\lambda^{\mathrm{HS}}$ and $r_o=5\lambda^{\mathrm{HS}}$. These conditions give Kn=0.447 (based on our definition for Knudsen number), while different accommodation factors are employed.

Plots (a) and (b) in Fig. 4 present Navier-Stokes results for velocity with first- and second-order slip conditions, respectively. It is shown that the new second-order slip condition improves the Navier-Stokes predictions and makes them comparable with DSMC and with the R13 results, which are depicted in plot (c). This improvement is more apparent near the outer stationary wall. For fully diffusive walls, the velocity profiles are compared in plot (d).

We emphasize that in the DSMC simulations of Ref. [18] the size of the gap between the cylinders is $2\lambda^{\mathrm{HS}}$, which is very small. The thickness of Knudsen boundary layers is usually in the order of two mean free paths. Therefore, in [18] the Knudsen layers affect the whole flow field, specifically for the diffusive walls. So we do not expect excellent agreement with the DSMC results of [18] since the Knudsen number is too large for our method. This motivated another comparison with DSMC data for smaller Knudsen number from Ref. [21].

In Ref. [21], unlike [18], the radius of the inner cylinder r_i is assigned as the characteristic length and $r_o=2r_i$. The dimensionless surface velocity of the inner cylinder is $\tilde{v}_\phi^{w,i}=\sqrt{2}/2$, and the outer cylinder is at rest. The Knudsen number k used in [21] is related to our definition by $k=8\sqrt{2}\ \mathrm{Kn}/(5\sqrt{\pi})$.

Figure 5 presents the velocity comparison for $\chi=\{0.01,0.2,1.0\}$ when $k=0.1$ or Kn=0.08. Since the Knudsen number is relatively small, the Navier-Stokes system shows good agreement. The profiles near the rotating wall are magnified to show the Knudsen layers. The R13 results exhibit more curvature than NSF due to the tangential heat flow effects.

B. Results for the temperature problem

As shown in Sec. III C, temperature and velocity problems are independent in the linearized systems. This means coupling between velocity and temperature fields (particularly, viscous heating) is ignored in our analysis. Therefore, the temperature problem is reduced to stationary radial heat conduction between the cylinders. DSMC simulations with isothermal cylinders [18,21] exhibit small temperature deviation due to viscous dissipation. Tibbs *et al.* [18] reported 1% and 3% density and temperature variations, respectively, while in Ref. [21] effects of viscous heating on density and temperature is about 5% for $k=0.1$.

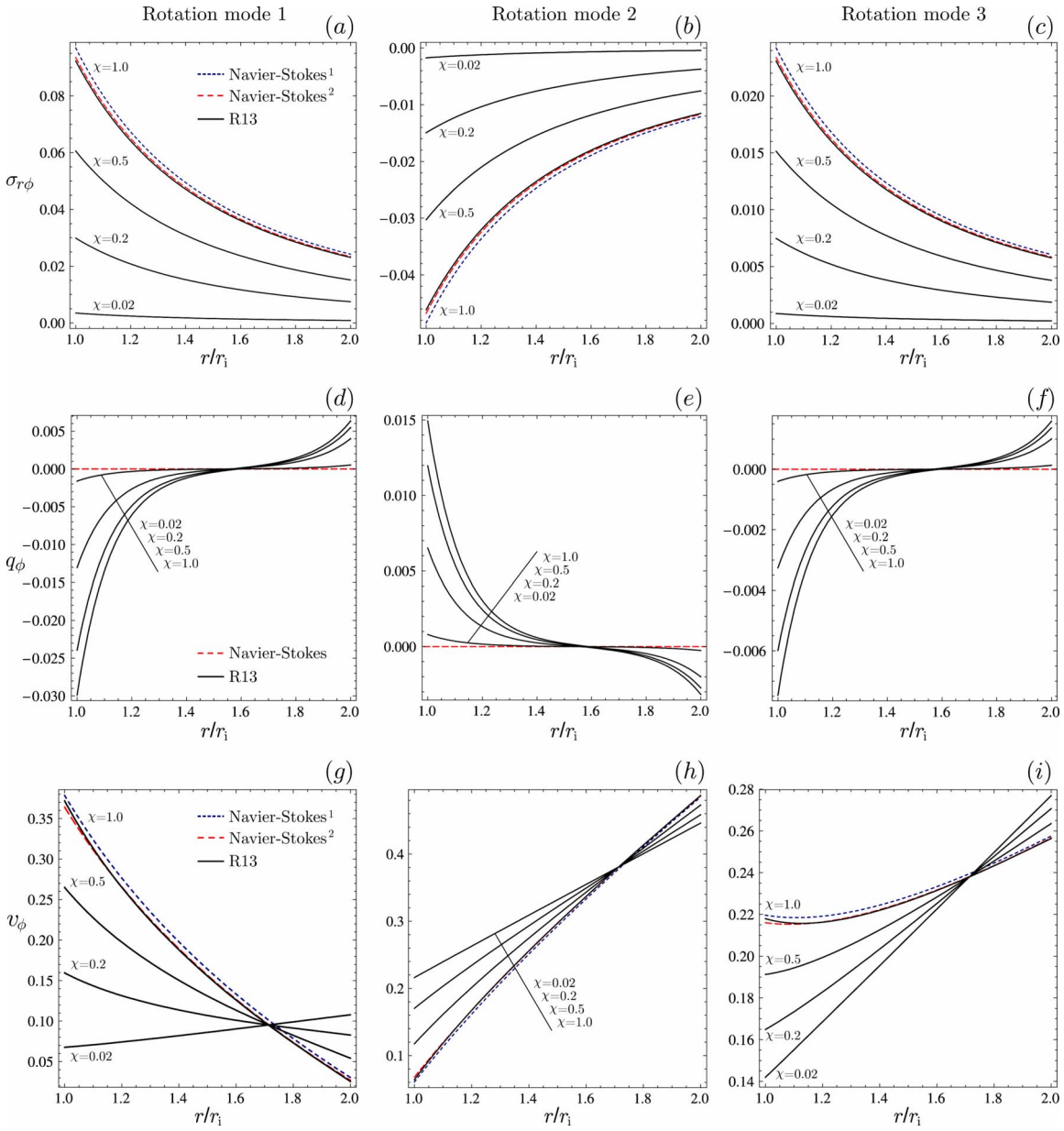

FIG. 3. (Color online) Solutions of the linear velocity problem: dashed blue line is NSF with first-order boundary condition; long-dashed red line is NSF with second-order boundary condition; continuous black line is R13 with third-order boundary conditions. Radial distribution of shear stress (top plots), circumferential heat flux (middle plots), and velocity (bottom plots) in the annulus for Kn=0.1 are shown. Plots in left, middle, and right columns correspond to rotational modes 1, 2, and 3, respectively. For each rotational mode, effects of surface accommodation factors are depicted. NSF results with the proposed second-order slip condition show satisfactory agreement with the R13 predictions. For the small Knudsen numbers NSF results are not shown, since they are very close to the R13 predictions.

As postulated by Fourier's law, for isothermal walls our numerical results for the linearized equations confirm a homogeneous radial distribution for temperature where,

$$\theta(r) = \theta^w, \quad q_r(r) = \sigma_{\phi\phi}(r) = \sigma_{rr}(r) = 0. \tag{63}$$

The above results, with Eq. (47), give a constant radial distribution for density $\varrho(r)=\varrho_0$.

We consider a case where the cylinders are at different temperatures. Then, the linear temperature problem can be characterized by Knudsen number Kn, surface accommodation factor χ, and wall temperatures θ^w. The parameters are chosen similar to the velocity problem, but $v_\phi^{w,i}=v_\phi^{w,o}=0$, and we shall define two temperature modes, with $\theta^{w,i}=2\theta^{w,o}=2$ and $\theta^{w,o}=2\theta^{w,i}=2$ for mode 1 and 2, respectively.

Profiles of diagonal elements of stress tensor, radial heat flux, and temperature are shown in Fig. 6. Plots (a)–(h) are obtained for fully diffusive walls $\chi=1$, and the effects of Kn variations are shown. Plots (i)–(p) are obtained for Kn=0.1, while the effects of χ variations are examined.

In the temperature problem switching between the temperature modes only inverts the process, compare the signs of σ_{rr}, $\sigma_{\phi\phi}$, and q_r between the temperature modes.

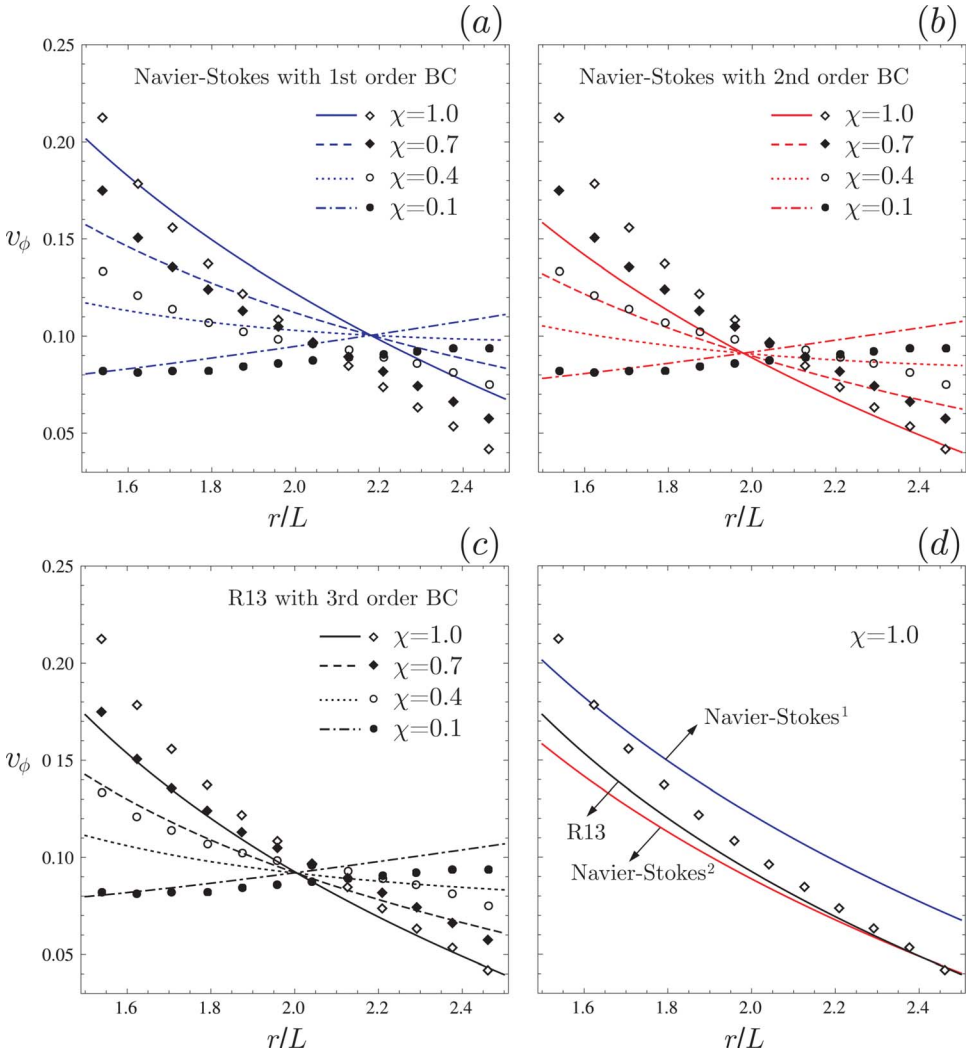

FIG. 4. (Color online) Radial velocity distribution for different accommodation factors when Kn=0.447. Knudsen number is defined based on the gap size, $L=r_o-r_i$. Navier-Stokes and R13 results are compared to DSMC data (diamond symbols) from Ref. [18].

The first and second row of plots show that diagonal stress components, which are zero in NSF system, grow with Kn and χ. These non-Newtonian stress components can be interpreted as Knudsen layers for the temperature problem. The behavior of radial heat flux q_r is similar to shear stress in the velocity problem. So one might conclude that in the linear limit the differences between the NSF and R13 results for q_r only refers to the difference between the boundary conditions. This cannot be proved through the numerical solutions as we do not have explicit solution for q_r. Heat flow between two cylinders is stronger at rarefied conditions due to the larger mean free path. Analogously, diffusive walls increase the heat flow since they provide better thermalization for the gas molecules.

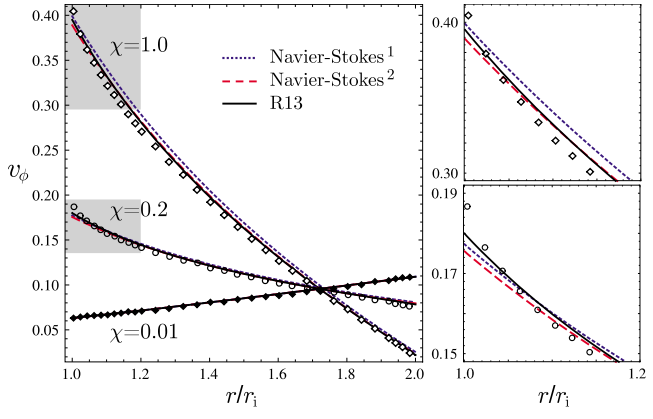

FIG. 5. (Color online) Radial velocity distribution for Kn =0.08 with different accommodation factors. Knudsen number is defined based on the radius of the inner cylinder. Navier-Stokes and R13 results are compared to DSMC data (symbols) from Ref. [21]. Profiles near the rotary wall (shaded areas) are magnified to show the effects of Knudsen layers.

The bottom plots in Fig. 6 are devoted to the radial temperature distribution. It can be seen that there are larger temperature jumps on the inner cylinder, owing to its higher curvature. Plots (g) and (h) show that temperature jump increases with Kn, since the number of gas-surface collisions decreases for large Knudsen numbers. On the other hand, temperature jump and χ are in inverse relation. For very small values of χ, temperature jump increases on both cylinders, such that a homogeneous temperature fills the annulus, see plots (o) and (p).

As shown in the plots, the proposed second-order jump condition provides better matching between NSF and R13 results. Indeed, the differences between the improved NSF

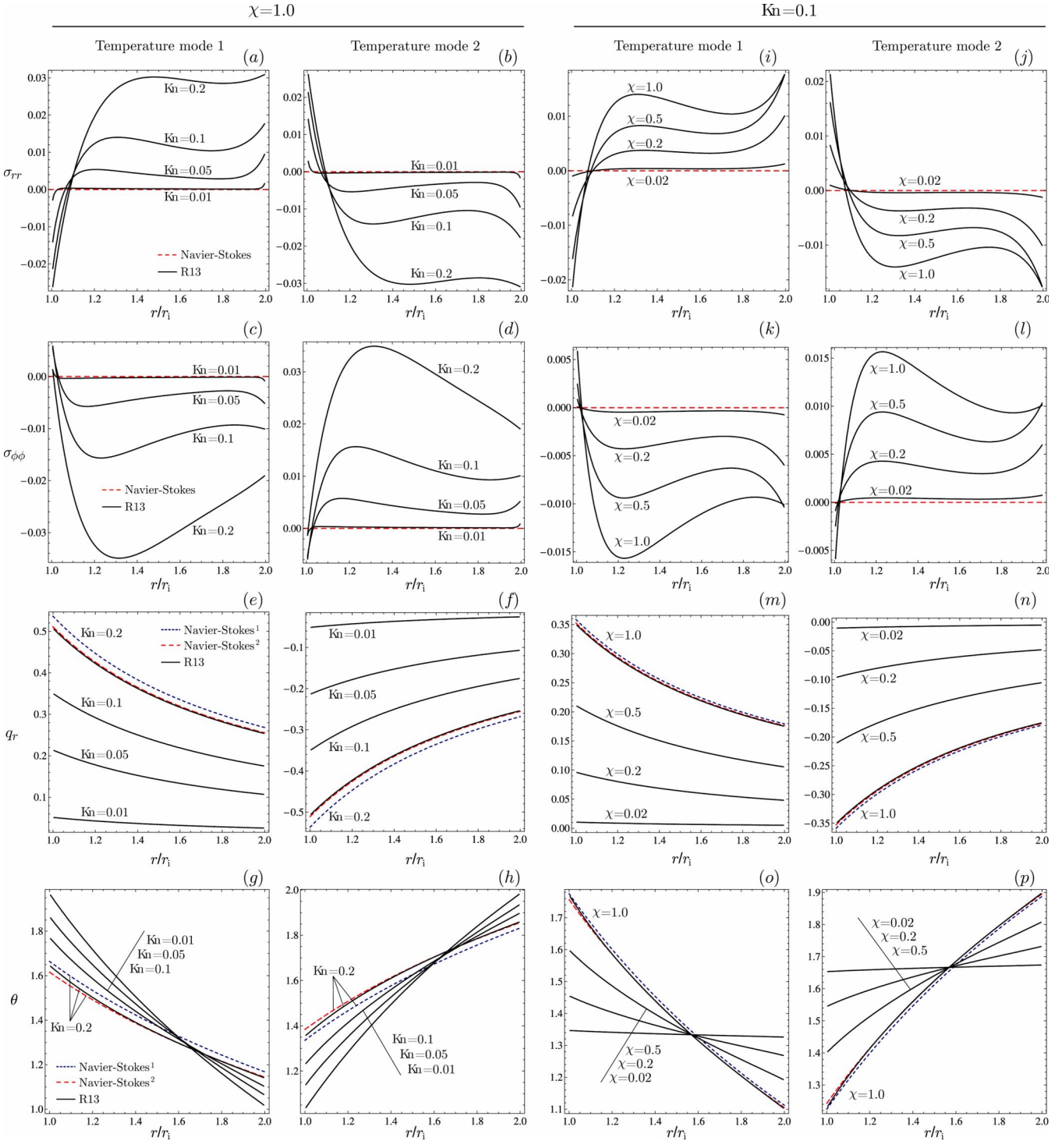

FIG. 6. (Color online) Solutions for the linear temperature problem: dashed blue line is NSF with first-order boundary condition; long-dashed red line is NSF with second-order boundary condition; continues black line is R13 with third-order boundary conditions. Radial distribution of non-Newtonian shear stresses (first and second rows), radial heat flux (third row), and temperature (bottom plots) in the annulus are shown. For each temperature mode, effects of different surface accommodation factors and Knudsen numbers are depicted.

and R13 predictions in temperature refers to the effects on Knudsen layers, compare Eq. (40) with Eq. (45).

Nonisothermal Couette flow between two rotating cylinders is investigated by Sharipov and Kremer [19] using the discrete velocity method for the BGK equation. In their simulations coupling between velocity and temperature fields is taken into account, which includes interaction of bulk flow and velocity and temperature Knudsen layers. Comparison of our data with those in [19] requires recasting the R13 equations for the BGK model followed by numerical solution for the fully nonlinear equations, which is currently under investigation and will be presented elsewhere.

VI. CONCLUSIONS

Cylindrical Couette flow and stationary heat transfer between coaxial cylinders were investigated with classical and extended hydrodynamics, Navier-Stokes-Fourier, and regularized 13-moment equations. The linear regime was considered, where velocity slip, temperature jump, and Knudsen layers are dominant rarefaction effects. In the velocity problem explicit expressions for Knudsen layers were obtained. Similar to Couette flows in slab geometry, these kinetic layers, which construct the circumferential heat flow, improve the curvature of R13 solutions near the boundaries as compared to solutions of the Boltzmann equation. Furthermore, we presented numerical solutions of Knudsen layers in the temperature problem, i.e., diagonal components of the stress tensor.

In the linear limit, the major difference between the planar and cylindrical cases is the coupling between σ_{rr} and $\sigma_{\phi\phi}$ within the geometry terms, which demands numerical tools for the temperature problem.

Moreover, a new set of second-order velocity slip and temperature jump conditions for Navier-Stokes-Fourier system was introduced. It was shown that the proposed boundary conditions effectively improve the NSF predictions.

ACKNOWLEDGMENT

This research was supported by the Natural Sciences and Engineering Research Council (NSERC).

APPENDIX A: SECOND-ORDER SLIP AND JUMP CONDITIONS IN CYLINDRICAL GEOMETRY

In order to derive second-order boundary conditions for Navier-Stokes-Fourier system consider R13 boundary conditions for $\sigma_{r\phi}$ and q_r, i.e., Eqs. (20) and (22), to find velocity slip and temperature jump as

$$\mathcal{V}_\phi = -\frac{2-\chi}{\chi}\sqrt{\frac{\pi\theta}{2}}\frac{\sigma_{r\phi}}{\mathcal{P}}n_r - \frac{1}{5}\frac{q_\phi}{\mathcal{P}} - \frac{1}{2}\frac{m_{rr\phi}}{\mathcal{P}} \tag{A1}$$

and

$$\mathcal{T} = -\frac{2-\chi}{\chi}\sqrt{\frac{\pi\theta}{2}}\frac{q_r}{2\mathcal{P}}n_r + \frac{1}{4}\mathcal{V}^2 - \frac{1}{4}\frac{\theta\sigma_{rr}}{\mathcal{P}} - \frac{1}{30}\frac{\Delta}{\mathcal{P}} - \frac{5}{56}\frac{R_{rr}}{\mathcal{P}}. \tag{A2}$$

The underlined terms represent the well-known first-order contributions to slip and jump, where $\sigma_{r\phi}$ and q_r need to be replaced from Eq. (19) and $\mathcal{P}^{\mathrm{NSF}}=p$. The rest are higher-order terms which are zero in NSF, however, they can be expressed in terms of Navier-Stokes and Fourier laws. To do so, we use a scaling approach based on the Chapman-Enskog expansion as in Ref. [41].

The equilibrium quantities density, temperature, and velocity are not expanded since they are of zeroth order. Normal heat flux and tangential stress are first-order quantities

$$q_r = \mathrm{Kn}\ \overset{*}{q}_r, \quad \sigma_{r\phi} = \mathrm{Kn}\ \overset{*}{\sigma}_{r\phi}, \tag{A3}$$

while second-order quantities are

$$q_\phi = \mathrm{Kn}^2\ \overset{*}{q}_\phi, \quad \sigma_{rr} = \mathrm{Kn}^2\ \overset{*}{\sigma}_{rr}, \quad \sigma_{\phi\phi} = \mathrm{Kn}^2\ \overset{*}{\sigma}_{\phi\phi},$$

$$\Delta = \mathrm{Kn}\ \overset{*}{\Delta}, \quad R_{rr} = \mathrm{Kn}^2\ \overset{*}{R}_{rr}, \quad R_{\phi\phi} = \mathrm{Kn}^2\ \overset{*}{R}_{\phi\phi},$$

$$m_{rr\phi} = \mathrm{Kn}^2\ \overset{*}{m}_{rr\phi}, \quad m_{\phi\phi\phi} = \mathrm{Kn}^2\ \overset{*}{m}_{\phi\phi\phi}. \tag{A4}$$

The remaining quantities which promote the R13 boundary conditions to be of third order are

$$R_{r\phi} = \mathrm{Kn}^3\ \overset{*}{R}_{r\phi},$$

$$m_{rrr} = \mathrm{Kn}^3\ \overset{*}{m}_{rrr}, \quad m_{r\phi\phi} = \mathrm{Kn}^3\ \overset{*}{m}_{r\phi\phi}. \tag{A5}$$

The moments in Eqs. (A3)–(A5) are scaled as $M=\mathrm{Kn}^\alpha\ \overset{*}{M}$, where the rescaled moment $\overset{*}{M}$ is of order unity and α is the order of the moment M.

Replacement of the scaled moments into the extended balance Eqs. (6)–(18) allows to reduce them up to second order. Accordingly, normal heat flux and shear stress balance reduce to the Fourier and Navier-Stokes laws

$$\overset{*}{q}_r = -\frac{15}{4}\mu\frac{\partial\theta}{\partial r}, \quad \overset{*}{\sigma}_{r\phi} = -\mu\left(\frac{\partial v_\phi}{\partial r} - \frac{v_\phi}{r}\right), \tag{A6}$$

and the required second-order moments read

$$\overset{*}{q}_\phi = -3\frac{\mu}{p}\left(\frac{\overset{*}{q}_r}{r} + \frac{1}{2}\frac{v_\phi\overset{*}{\sigma}_{r\phi}}{r}\right)v_\phi + \frac{7}{2}\frac{\overset{*}{q}_r\overset{*}{\sigma}_{r\phi}}{p} - 3\frac{\mu\theta}{p}\left(\frac{1}{2}\frac{\partial\overset{*}{\sigma}_{r\phi}}{\partial r} + \frac{\overset{*}{\sigma}_{r\phi}}{r}\right), \tag{A7}$$

$$\overset{*}{\sigma}_{rr} = 4\frac{\mu}{p}\left(\frac{v_\phi\overset{*}{\sigma}_{r\phi}}{r} + \frac{1}{5}\frac{\overset{*}{q}_r}{r}\right) - \frac{6}{5}\frac{\overset{*2}{\sigma}_{r\phi}}{p}, \tag{A8}$$

$$\overset{*}{\sigma}_{\phi\phi} = -4\frac{\mu}{p}\left(\frac{v_\phi\overset{*}{\sigma}_{r\phi}}{r} + \frac{1}{5}\frac{\overset{*}{q}_r}{r}\right) + \frac{8}{5}\frac{\overset{*2}{\sigma}_{r\phi}}{p}, \tag{A9}$$

$$\overset{*}{\Delta} = 12\frac{\mu\theta}{p}\left(\frac{1}{\theta}\frac{v_\phi^2\overset{*}{q}_r}{r} - \frac{\partial\overset{*}{q}_r}{\partial r} - \frac{\overset{*}{q}_r}{r}\right) + 10\frac{\theta\overset{*2}{\sigma}_{r\phi}}{p} + \frac{56}{5}\frac{\overset{*2}{q}_r}{p}, \tag{A10}$$

$$\overset{*}{R}_{rr} = \frac{16}{5}\frac{\mu\theta}{p}\left(\frac{1}{\theta}\frac{v_\phi^2\overset{*}{q}_r}{r} - \frac{\partial\overset{*}{q}_r}{\partial r} + \frac{1}{2}\frac{\overset{*}{q}_r}{r}\right) + \frac{20}{21}\frac{\theta\overset{*2}{\sigma}_{r\phi}}{p} + \frac{128}{75}\frac{\overset{*2}{q}_r}{p}, \tag{A11}$$

$$\overset{*}{m}_{rr\phi} = \frac{16}{15}\frac{\mu\theta}{p}\left(\frac{1}{\theta}\frac{v_\phi^2\overset{*}{\sigma}_{r\phi}}{r} - \frac{\partial\overset{*}{\sigma}_{r\phi}}{\partial r} + \frac{7}{4}\frac{\overset{*}{\sigma}_{r\phi}}{r}\right) + \frac{32}{45}\frac{\overset{*}{q}_r\overset{*}{\sigma}_{r\phi}}{p}. \tag{A12}$$

Since the moments in Eq. (A5) yield third- and higher-order terms, they will be discarded and their equations are not shown here.

Substitution of Eqs. (A7)–(A12) into Eqs. (A1) and (A2) gives the second order slip and jump conditions, as presented

in the text, i.e., Eqs. (27) and (28). The last step includes replacement of Eq. (A6) into the obtained boundary conditions.

APPENDIX B: DIMENSIONLESS PARAMETERS

The reference equilibrium state is defined by $\{\varrho_0, \theta_0, v_i^0=0\}$. The non-dimensional radial coordinate and time are defined as

$$\tilde{r} = \frac{r}{\ell} \quad \text{and} \quad \tilde{t} = \frac{\sqrt{\theta_0}}{\ell} t, \tag{B1}$$

where the arbitrary macroscopic length scale and thermal speed at reference state are denoted by ℓ and $\sqrt{\theta_0}$, respectively. The hat signs indicate dimensionless quantities, which for better readability are removed in the text. Nondimensional density and temperature are defined as deviations from the reference state,

$$\tilde{\varrho} = \frac{\varrho - \varrho_0}{\varrho_0} \quad \text{and} \quad \tilde{\theta} = \frac{\theta - \theta_0}{\theta_0}. \tag{B2}$$

Accordingly, equation of state for the ideal gases reads

$$p = \varrho\theta = \varrho_0\theta_0(1+\tilde{\varrho})(1+\tilde{\theta}) = p_0(1+\tilde{\varrho}+\tilde{\theta}), \tag{B3}$$

where $\tilde{\varrho}\tilde{\theta}=0$ in linearization.

The other dimensionless variables are

$$\tilde{v}_i = \frac{v_i}{\sqrt{\theta_0}}, \quad \tilde{\sigma}_{ij} = \frac{\sigma_{ij}}{\varrho_0\theta_0}, \quad \tilde{q}_i = \frac{q_i}{\varrho_0\sqrt{\theta_0}^3},$$

$$\tilde{\Delta} = \frac{\Delta}{\varrho_0\theta_0^2}, \quad \tilde{R}_{ij} = \frac{R_{ij}}{\varrho_0\theta_0^2}, \quad \tilde{m}_{ijk} = \frac{m_{ijk}}{\varrho_0\sqrt{\theta_0}^3}. \tag{B4}$$

Moreover, the dimensionless viscosity $\tilde{\mu}$ is defined as

$$\tilde{\mu} = \frac{\mu}{\mu_0}, \quad \text{where} \quad \mu_0 = \mu(\theta_0). \tag{B5}$$

In the governing equations, wherever we have viscosity, the dimensionless equations will include the reference Knudsen number Kn,

$$\mathrm{Kn} = \frac{\lambda_0}{\ell} = \frac{\mu_0\sqrt{\theta_0}}{p_0\ell}. \tag{B6}$$

[1] C. Cercignani, *Theory and Application of the Boltzmann Equation* (Scottish Academic Press, London, 1975).
[2] Y. Sone, *Kinetic Theory and Fluid Dynamics* (Birkhäuser, Boston, 2002).
[3] V. Garzó and A. Santos, *Kinetic Theory of Gases in Shear Flows* (Kluwer, Dordrecht, 2003).
[4] H. Struchtrup, *Macroscopic Transport Equations for Rarefied Gas Flows: Approximation Methods in Kinetic Theory* (Springer, New York, 2005).
[5] S. K. Loyalka, Phys. Fluids **18**, 1666 (1975).
[6] Y. Sone, T. Ohwada, and K. Aoki, Phys. Fluids A **1**, 363 (1989).
[7] S. K. Loyalka, Phys. Fluids A **1**, 403 (1989).
[8] T. Ohwada, Y. Sone, and K. Aoki, Phys. Fluids A **1**, 1588 (1989).
[9] S. L. Dixon, *Fluid Mechanics and Thermodynamics of Turbomachinery* (Elsevier BH, Oxford, 1998).
[10] R. Gohar and H. Rahnejat, *Fundamentals of Tribology* (Imperial College Press, London, 2008).
[11] D. J. Alofs and G. S. Springer, Rev. Sci. Instrum. **41**, 1161 (1970).
[12] D. J. Alofs and G. S. Springer, Phys. Fluids **14**, 298 (1971).
[13] C. Cercignani and F. Sernagiotto, Phys. Fluids **10**, 1200 (1967).
[14] K. Nanbu, Phys. Fluids **27**, 2632 (1984).
[15] S. Stefanov and C. Cercignani, J. Fluid Mech. **256**, 199 (1993).
[16] F. M. Sharipov and G. M. Kremer, Transp. Theory Stat. Phys. **25**, 217 (1996).
[17] Y. Sone, S. Takata, and H. Sugimoto, Phys. Fluids **8**, 3403 (1996).
[18] K. W. Tibbs, F. Baras, and A. L. Garcia, Phys. Rev. E **56**, 2282 (1997).
[19] F. M. Sharipov and G. M. Kremer, Eur. J. Mech. B/Fluids **18**, 121 (1999).
[20] Y. Sone, H. Sugimoto, and K. Aoki, Phys. Fluids **11**, 476 (1999).
[21] K. Aoki, H. Yoshida, T. Nakanishi, and A. L. Garcia, Phys. Rev. E **68**, 016302 (2003).
[22] Y. Sone and T. Doi, Phys. Fluids **16**, 952 (2004).
[23] H. Yoshida and K. Aoki, Phys. Rev. E **73**, 021201 (2006).
[24] P. L. Bhatnagar, E. P. Gross, and M. Krook, Phys. Rev. **94**, 511 (1954).
[25] A. Bird, *Molecular Gas Dynamics and the Direct Simulation of Gas Flows* (Oxford University Press, New York, 1998).
[26] D. Einzel, P. Panzer, and M. Liu, Phys. Rev. Lett. **64**, 2269 (1990).
[27] S. Yuhong, R. W. Barber, and D. R. Emerson, Phys. Fluids **17**, 047102 (2005).
[28] R. S. Myong, J. M. Reese, R. W. Barber, and D. R. Emerson, Phys. Fluids **17**, 087105 (2005).
[29] S. Chapman and T. G. Cowling, *The Mathematical Theory of Nonuniform Gases* (Cambridge University Press, 1970).
[30] H. Grad, Commun. Pure Appl. Math. **2**, 331 (1949).
[31] H. Grad, in *Handbuch der Physik XII: Thermodynamik der Gase*, edited by S. Flügge (Springer, Berlin, 1958).
[32] T. C. Lin and R. E. Street, NASA Report No. 1175, 1954 (unpublished).
[33] A. V. Bobylev, Sov. Phys. Dokl. **27**, 29 (1982).
[34] P. Rosenau, Phys. Rev. A **40**, 7193 (1989).
[35] R. E. Khayat and B. C. Eu, Phys. Rev. A **38**, 2492 (1988).
[36] R. E. Khayat and B. C. Eu, Phys. Rev. A **39**, 728 (1989).
[37] H. Struchtrup and T. Thatcher, Continuum Mech. Thermodyn. **19**, 177 (2007).

[38] H. Struchtrup and M. Torrilhon, Phys. Rev. Lett. **99**, 014502 (2007).
[39] H. Struchtrup, Physica A **387**, 1750 (2008).
[40] M. Torrilhon and H. Struchtrup, J. Comput. Phys. **227**, 1982 (2008).
[41] H. Struchtrup and M. Torrilhon, Phys. Rev. E **78**, 046301 (2008).
[42] P. Taheri, M. Torrilhon, and H. Struchtrup, Phys. Fluids **21**, 017102 (2009).
[43] P. Taheri and H. Struchtrup (unpublished).
[44] H. Struchtrup and M. Torrilhon, Phys. Fluids **15**, 2668 (2003).
[45] H. Struchtrup, Phys. Fluids **16**, 3921 (2004).
[46] C. D. Andereck, S. S. Liu, and H. L. Swinney, J. Fluid Mech. **164**, 155 (1986).
[47] M. Itskov, *Tensor Algebra and Tensor Analysis for Engineers: With Applications to Continuum Mechanics* (Springer, New York, 2007).
[48] C. Truesdell and R. G. Muncaster, *Fundamentals of Maxwell's Kinetic Theory of A Simple Monatomic Gas* (Academic Press, New York, 1980).
[49] J. C. Maxwell, Philos. Trans. R. Soc. London, Ser. A **170**, 231 (1879).
[50] H. Struchtrup and W. Weiss, Continuum Mech. Thermodyn. **12**, 1 (2000).
[51] X. J. Gu and D. R. Emerson, J. Comput. Phys. **225**, 263 (2007).